

J1154+2443: a low-redshift compact star-forming galaxy with a 46 per cent leakage of Lyman continuum photons

Y. I. Izotov^{1,2}, D. Schaerer^{3,4}, G. Worseck^{5,6}, N. G. Guseva^{1,2}, T. X. Thuan⁷,
A. Verhamme³, I. Orlitová⁸ & K. J. Fricke^{9,2}

¹*Main Astronomical Observatory, Ukrainian National Academy of Sciences, 27 Zabolotnoho str., Kyiv 03143, Ukraine,
E-mail: izotov@mao.kiev.ua, guseva@mao.kiev.ua*

²*Max-Planck-Institut für Radioastronomie, Auf dem Hügel 69, D-53121 Bonn, Germany*

³*Observatoire de Genève, Université de Genève, 51 Ch. des Maillettes, 1290, Versoix, Switzerland,*

E-mail: daniel.schaerer@unige.ch, anne.verhamme@unige.ch

⁴*IRAP/CNRS, 14, Av. E. Belin, 31400 Toulouse, France*

⁵*Max-Planck-Institut für Astronomie, Königstuhl 17, D-69117 Heidelberg, Germany*

⁶*Institut für Physik und Astronomie, Universität Potsdam, Karl-Liebknecht-Str. 24/25, D-14476 Potsdam, Germany,*

E-mail: gworseck@uni-potsdam.de

⁷*Astronomy Department, University of Virginia, P.O. Box 400325, Charlottesville, VA 22904-4325, USA,*

E-mail: txt@virginia.edu

⁸*Astronomical Institute, Czech Academy of Sciences, Boční II 1401, 141 00, Prague, Czech Republic,*

E-mail: orlitova@asu.cas.cz

⁹*Institut für Astrophysik, Göttingen Universität, Friedrich-Hund-Platz 1, D-37077 Göttingen, Germany,*

E-mail: kfricke@gwdg.de

Accepted XXX. Received YYY; in original form ZZZ

ABSTRACT

We report the detection of the Lyman continuum (LyC) radiation of the compact star-forming galaxy (SFG) J1154+2443 observed with the Cosmic Origins Spectrograph (COS) onboard the *Hubble Space Telescope*. This galaxy, at a redshift of $z = 0.3690$, is characterized by a high emission-line flux ratio $O_{32} = [O\ III]\lambda 5007/[O\ II]\lambda 3727 = 11.5$. The escape fraction of the LyC radiation $f_{\text{esc}}(\text{LyC})$ in this galaxy is 46 per cent, the highest value found so far in low-redshift SFGs and one of the highest values found in galaxies at any redshift. The narrow double-peaked Ly α emission line is detected in the spectrum of J1154+2443 with a separation between the peaks V_{sep} of 199 km s^{-1} , one of the lowest known for Ly α -emitting galaxies, implying a high $f_{\text{esc}}(\text{Ly}\alpha)$. Comparing the extinction-corrected Ly α /H β flux ratio with the case B value we find $f_{\text{esc}}(\text{Ly}\alpha) = 98$ per cent. Our observations, combined with previous detections in the literature, reveal an increase of O_{32} with increasing $f_{\text{esc}}(\text{LyC})$. We also find a tight anticorrelation between $f_{\text{esc}}(\text{LyC})$ and V_{sep} . The surface brightness profile derived from the COS acquisition image reveals a bright star-forming region in the centre and an exponential disc in the outskirts with a disc scale length $\alpha = 1.09$ kpc. J1154+2443, compared to other known low-redshift LyC leakers, is characterized by the lowest metallicity, $12+\log O/H = 7.65 \pm 0.01$, the lowest stellar mass $M_{\star} = 10^{8.20} M_{\odot}$, a similar star formation rate $\text{SFR} = 18.9 M_{\odot} \text{ yr}^{-1}$ and a high specific SFR of $1.2 \times 10^{-7} \text{ yr}^{-1}$.

Key words: (cosmology:) dark ages, reionization, first stars — galaxies: abundances — galaxies: dwarf — galaxies: fundamental parameters — galaxies: ISM — galaxies: starburst

1 INTRODUCTION

It is commonly accepted that star-forming galaxies were the main contributors to the reionization of the Universe after the cosmic Dark Ages, when the baryonic matter was neutral. While Madau & Haardt (2015) considered active galactic nuclei (AGN) as possible alternative sources of the

ionization, more recent studies (Hassan et al. 2018; Mitra, Choudhury & Ferrara 2013) show that the contribution of AGNs to the reionization of the Universe was small. However, the currently identified relatively bright star-forming galaxies (SFGs) are insufficient to fully ionize the Universe by redshift $z \sim 6$ (Steidel, Pettini & Adelberger 2001; Cowie,

Barger & Trouille 2009; Iwata et al. 2009; Robertson et al. 2013), and it is generally thought that numerous fainter low-mass SFGs, below the current detection limit of observations, are responsible for the bulk of the ionizing radiation at $z \gtrsim 6$ (Ouchi et al. 2009; Wise & Chen 2009; Mitra, Ferrara & Choudhury 2013; Yajima, Choi & Nagamine 2011; Bouwens et al. 2015). Additionally, for galaxies to reionize the Universe, the escape fraction of their ionizing radiation has to be sufficiently high, of the order of 10–20 per cent (e.g. Ouchi et al. 2009; Robertson et al. 2013; Dressler et al. 2015; Robertson et al. 2015; Khaire et al. 2016).

Generally, searches for Lyman continuum (LyC) leakers, both at high and low redshifts, have so far been difficult and largely unsuccessful. Over the past, deep imaging studies at $z \sim 3$ have produced several candidate LyC leaking galaxies (e.g. Steidel et al. 2001; Iwata et al. 2009; Nestor et al. 2011; Mostardi et al. 2013), whereas other teams have only obtained stringent upper limits (e.g. Vanzella et al. 2010; Boutsia et al. 2011). Currently, the most reliable LyC leakers detected at high redshift are the objects *Ion2* ($z = 3.212$, Vanzella et al. 2015; de Barros et al. 2016) with a relative escape fraction $f_{\text{esc}}^{\text{rel}}(\text{LyC}) = 0.64^{+1.1}_{-0.1}$, Q1549-C25 ($z = 3.212$, Shapley et al. 2016) with $f_{\text{esc}}(\text{LyC}) > 0.51$, and A2218-Flanking ($z \approx 2.5$, Bian et al. 2017) with $f_{\text{esc}}(\text{LyC}) > 0.28 - 0.57$.

Since direct observations of high-redshift galaxies are difficult because of their faintness, contamination by lower-redshift interlopers, and the increase of intergalactic medium (IGM) opacity (e.g., Vanzella et al. 2010, 2012; Inoue et al. 2014; Grazian et al. 2016), it is important to identify and study local proxies of this galaxy population. However, starburst galaxies at low redshifts are generally opaque to their ionizing radiation (Leitherer et al. 1995; Deharveng et al. 2001; Grimes et al. 2009). This radiation was directly detected only in four low-redshift galaxies, with small escape fractions $f_{\text{esc}}(\text{LyC})$ of $\sim 1 - 4.5$ per cent. Two of these galaxies were observed with the *Hubble Space Telescope* (*HST*)/Cosmic Origins Spectrograph (COS) (Borthakur et al. 2014; Leitherer et al. 2016), one galaxy with the *Far Ultraviolet Spectroscopic Explorer* (*FUSE*) (Leitet et al. 2013) and one galaxy with both the *HST*/COS and *FUSE* (Leitet et al. 2013; Leitherer et al. 2016).

However, we note that according to the recent re-analysis of $f_{\text{esc}}(\text{LyC})$ by Chisholm et al. (2017) in low-redshift galaxies observed with COS, only the galaxy of Borthakur et al. (2014) is found to be a definite LyC leaker. As for the galaxies discussed by Leitherer et al. (2016), Mrk 54 is not a LyC leaker according to Chisholm et al. (2017), Tol 0440–381 and Tol 1247–232 are detected at the $\sim 2\sigma$ level, but these detections could be affected by residual geocoronal emission. Furthermore, the COS spectrum of Tol 1247–232 reveals a significantly lower $f_{\text{esc}}(\text{LyC})$ than the earlier *FUSE* data by Leitet et al. (2013) (0.4 per cent instead of 2.4 per cent). Haro 11 was observed only with *FUSE* (Leitet et al. 2013) and has still to be confirmed with COS observations.

It was recently argued that low-mass compact galaxies at low redshifts $z < 1$ with very active star formation may be promising candidates for escaping ionizing radiation (Jaskot & Oey 2013; Stasińska et al. 2015). The subsample of these galaxies in the redshift range $z \sim 0.1 - 0.3$ is often referred to as “Green Pea” (GP) galaxies because of their green colour

Table 1. Coordinates, redshift, O_{32} ratio and apparent magnitudes of J1154+2443

R.A.(2000.0)	11:54:48.85
Dec.(2000.0)	+24:43:33.03
z	0.3690
O_{32}	11.5
SDSS u (mag)	22.01±0.16
SDSS g (mag)	21.77±0.05
SDSS r (mag)	21.97±0.09
SDSS i (mag)	21.99±0.13
SDSS z (mag)	21.04±0.24
<i>GALEX FUV</i> (mag)	22.10±0.53
<i>GALEX NUV</i> (mag)	21.57±0.34

in the composite SDSS images (Cardamone et al. 2009). On the other hand, Izotov, Guseva & Thuan (2011) have named all galaxies in the wider redshift range $\sim 0.0 - 0.6$ with an $\text{H}\beta$ emission-line luminosity $L(\text{H}\beta) \gtrsim 10^{40.5} \text{ erg s}^{-1}$ as Luminous Compact Galaxies (LCG). The general characteristic of compact SFGs, including both GPs and LCGs, is the presence of strong emission lines in the optical spectra of their H II regions, powered by numerous O-stars which produce plenty of ionizing radiation.

Izotov et al. (2015, 2016c), using SDSS data, selected ~ 15000 compact SFGs at $z < 1$ and studied their properties. They found that in general these galaxies are low-mass and low-metallicity galaxies. Their stellar masses, star formation rates (SFR) and metallicities are similar to those of high-redshift Lyman-alpha emitting (LAE) and Lyman-break galaxies (LBG) (Izotov et al. 2015). Many compact SFGs are characterised by high line ratios $\text{O}_{32} = [\text{O III}]\lambda 5007/[\text{O II}]\lambda 3727 \gtrsim 5$, reaching values of up to 60 in some galaxies (Stasińska et al. 2015). Such high values may indicate that H II regions are density-bounded, allowing escape of ionizing radiation to the IGM, as suggested e.g. by Jaskot & Oey (2013) and Nakajima & Ouchi (2014). Indeed, Izotov et al. (2016a,b), using *HST*/COS observations of five compact SFGs at redshift $z \sim 0.3$ and with $\text{O}_{32} = 5 - 8$, found that all these galaxies are leaking LyC radiation, with an escape fraction of 6 – 13 per cent.

Based on the unique properties of compact SFGs and the success of our previous observations (Izotov et al. 2016a,b), we selected an additional sample of 6 more galaxies, covering a range of $\text{O}_{32} > 10$. J1154+2443 is the first of these galaxies that have been selected for spectroscopic observations with the *HST*, in conjunction with the COS. Our aim is to detect escaping ionizing radiation shortward of the Lyman continuum limit, at rest wavelengths $\lesssim 912\text{\AA}$, and the $\text{Ly}\alpha$ emission line of this galaxy.

The results of these observations are presented in this paper. The selection criteria are discussed in Section 2. Extinction in the optical range and element abundances are discussed in Section 3. The *HST* observations and data reduction are described in Section 4. We derive the surface brightness profile in the near-ultraviolet (NUV) range in Section 5. Integrated characteristics of J1154+2443 are derived in Section 6. $\text{Ly}\alpha$ emission is considered in Section 7. The Lyman continuum detection and the corresponding escape fractions are presented in Section 8. Finally, we summarize our findings in Section 9.

Table 2. Extinction-corrected emission-line fluxes and equivalent widths in the SDSS spectrum

Line	λ	$I^{a,b}$	$I^{a,c}$	EW_{obs}^d
Mg II	2796	15.8±2.4	11.9±1.8	5
Mg II	2803	9.7±1.9	7.3±1.5	4
[O II]	3727	60.5±4.0	50.4±3.5	44
H9	3836	10.8±3.9	9.3±3.4	8
[Ne III]	3869	48.2±3.5	42.8±3.1	33
H8+He I	3889	24.4±4.0	21.4±3.5	20
H7+[Ne III]	3969	30.1±4.2	26.7±2.7	25
H δ	4101	30.3±4.1	27.3±3.7	26
H γ	4340	50.7±3.9	47.4±3.7	74
[O III]	4363	17.8±2.4	16.8±2.2	19
He I	4471	5.7±2.8	5.5±2.3	11
H β	4861	100.0±5.1	100.0±5.0	220
[O III]	4959	194.2±7.5	196.5±7.5	466
[O III]	5007	568.0±16.	577.5±16.	1121
He I	5876	10.8±1.8	11.7±1.9	33
H α	6563	281.5±11.	318.7±12.	1150
[N II]	6583	3.5±1.8	3.9±2.0	10
[S II]	6717	4.6±1.5	5.3±1.7	16
[S II]	6731	5.4±1.3	6.2±1.5	22
He I	7065	10.6±2.1	12.4±2.5	65
$C(\text{H}\beta)^e$		0.250	0.070	
$I(\text{H}\beta)^f$		13.8	9.1	

^a $I = 100 \times I(\lambda) / I(\text{H}\beta)$, where $I(\lambda)$ and $I(\text{H}\beta)$ are emission-line fluxes, corrected for both the Milky Way and internal extinction.

^bCorrected for internal extinction with $C(\text{H}\beta) = 0.25$ derived from the observed Balmer decrement including H α .

^cCorrected for internal extinction with $C(\text{H}\beta) = 0.07$ derived from the observed Balmer decrement excluding H α .

^dObserved equivalent width in Å.

^eInternal extinction.

^fin 10^{-16} erg s $^{-1}$ cm $^{-2}$.

2 SELECTION CRITERIA

The galaxy J1154+2443 was chosen from the sample of compact SFGs selected from the SDSS Data Release 10 (DR10) (Ahn et al. 2014). The following selection criteria were applied to construct the sample (Izotov et al. 2015): 1) the angular galaxy radius on the SDSS images $R_{50} \leq 3$ arcsec, where R_{50} is the galaxy’s Petrosian radius within which 50 per cent of the galaxy’s flux in the SDSS r band is contained; 2) a high equivalent width $EW(\text{H}\beta) \gtrsim 50$ Å of the H β emission line in the SDSS spectrum; this ensures very recent star formation with an age of 2 – 3 Myr and the presence of numerous hot O stars producing copious amounts of ionizing LyC radiation. Additionally, for the *HST* observations, the following criteria were applied: 1) a sufficiently high brightness in the far-ultraviolet (FUV) and a high enough redshift ($z \gtrsim 0.3$) to allow direct LyC observations with the COS; and 2) a high extinction-corrected $O_{32} \gtrsim 5$, which may indicate the presence of density-bounded H II regions, i.e. escaping LyC radiation (Jaskot & Oey 2013; Nakajima & Ouchi 2014; Izotov, Thuan & Guseva 2017).

J1154+2443 fulfils all the above criteria. In particular, its O_{32} of 11.5 is the highest compared to all low-redshift LyC leakers observed so far with the *HST*/COS.

The coordinates, redshift, and O_{32} ratio of J1154+2443 and its SDSS and *GALEX* apparent magnitudes are shown in Table 1.

Table 3. Electron temperatures, electron number density and element abundances

Parameter	Value ^a	Value ^b
T_e ([O III]), K	19100±1500	18300±1400
T_e ([O II]), K	15500±1100	15300±1100
N_e ([S II]), cm $^{-3}$	1200±1000	1200±1000
$O^+ / H^+ \times 10^5$	0.56±0.04	0.51±0.04
$O^{2+} / H^+ \times 10^5$	3.59±0.09	4.00±0.09
$O / H \times 10^5$	4.15±0.10	4.51±0.10
$12 + \log O / H$	7.62±0.01	7.65±0.01
$N^+ / H^+ \times 10^6$	0.24±0.13	0.28±0.15
ICF(N) ^c	6.93	8.20
$N / H \times 10^6$	1.67±0.96	2.28±1.33
$\log N / O$	-1.40±0.25	-1.30±0.25
$Ne^{2+} / H^+ \times 10^5$	0.68±0.06	0.67±0.06
ICF(Ne) ^c	1.06	1.04
$Ne / H \times 10^5$	0.72±0.06	0.70±0.06
$\log Ne / O$	-0.76±0.04	-0.81±0.04
$Mg^+ / H^+ \times 10^7$	1.47±0.25	1.17±0.19
ICF(Mg) ^c	13.69	15.79
$Mg / H \times 10^6$	2.01±0.34	1.84±0.30
$\log Mg / O$	-1.31±0.07	-1.38±0.07

^aFor the internal extinction $C(\text{H}\beta) = 0.25$.

^bFor the internal extinction $C(\text{H}\beta) = 0.07$.

^cIonization correction factor.

3 EXTINCTION IN THE OPTICAL RANGE AND ELEMENT ABUNDANCES

The SDSS spectrum of J1154+2443 is characterized by a blue continuum and strong nebular emission lines, indicating a young starburst with an age of $\sim 2 - 3$ Myr. The observed decrement of several hydrogen Balmer emission lines is used to correct the line fluxes for reddening according to Izotov, Thuan & Lipovetsky (1994) and adopting the reddening law by Cardelli, Clayton & Mathis (1989) which is parameterized by the ratio of total-to-selective extinction $R(V) = A(V)/E(B - V)$. The extinction coefficient $C(\text{H}\beta)$ derived from the hydrogen Balmer decrement corresponds to the extinction $A(\text{H}\beta) = 2.512 \times C(\text{H}\beta)$ at the H β wavelength. Then, adopting $R(V)$, the extinction $A(V)$ in the V band is derived from the relation $C(\text{H}\beta)/A(V) = f[R(V)]$ (Izotov et al. 2016a).

The correction for reddening was done in two steps. First, the observed spectrum, uncorrected for redshift, was corrected for the Milky Way extinction with $A(V)_{\text{MW}}$ from the NASA Extragalactic Database (NED)¹ and $R(V)_{\text{MW}} = 3.1$. Then, the rest-frame spectrum was corrected for the internal extinction of the galaxy, obtained from the hydrogen Balmer decrement. One would expect to derive similar internal extinction whether the H α emission line is included or not in the determination of $C(\text{H}\beta)$. However, for J1154+2443 we find very different $C(\text{H}\beta)$, of 0.250 with the

¹ NASA/IPAC Extragalactic Database (NED) is operated by the Jet Propulsion Laboratory, California Institute of Technology, under contract with the National Aeronautics and Space Administration.

$H\alpha$ emission line included and of 0.070 with the $H\alpha$ emission line excluded. Adopting the high value $C(H\beta) = 0.250$ for reddening correction would result in an overcorrection of the $H\delta/H\beta$ and $H\gamma/H\beta$ ratios by ~ 10 per cent compared to the case B values (Table 2). This indicates that the $H\alpha$ emission line might be enhanced by some non-recombination processes. One of the possible mechanisms would be the collisional excitation of the $H\alpha$ line in the dense H II region of J1154+2443 (see e.g. Izotov, Stasińska & Guseva 2013). Furthermore, the $H\alpha$ having an observed wavelength of 8986.8 Å and full width at half maximum of 6 Å, it could be affected by residuals of the relatively strong night sky emission lines with wavelengths 8982.3 Å, 8985.7 Å and 8988.3 Å (Hanuschik 2003).

The investigation of possible sources of the $H\alpha$ enhancement is not the main concern of this paper. Therefore, we will adopt an empirical approach: we will consider both values of the internal extinction coefficient, $C(H\beta) = 0.25$ and 0.07. We will then compare the observational data in the UV and optical ranges with our SED models to determine the most appropriate value of $C(H\beta)$.

The extinction-corrected emission-line fluxes relative to the $H\beta$ emission line flux and the observed equivalent widths are shown in Table 2 for both values of the internal extinction coefficient $C(H\beta)$, 0.25 and 0.07. The Table also gives $C(H\beta)$ and the $H\beta$ emission-line fluxes $I(H\beta)$ corrected for both the Milky Way and internal extinctions derived in the way described above. It is seen that the extinction-corrected $H\delta/H\beta$ and $H\gamma/H\beta$ flux ratios with $C(H\beta) = 0.07$ are very close to the case B values, while the $H\alpha/H\beta$ flux ratio is ~ 15 per cent above the theoretical value. On the other hand, adopting $C(H\beta) = 0.25$ we derived case B $H\alpha/H\beta$ flux ratio, but the $H\delta/H\beta$ and $H\gamma/H\beta$ flux ratios are ~ 10 per cent above the case B ratios.

We note that in the case of H II regions with non-negligible $f_{\text{esc}}(\text{LyC})$, the recombination flux ratios of Balmer hydrogen lines can deviate from the case B values. We check this possibility using the CLOUDY models (Ferland et al. 1998, 2013) with different column densities $N(\text{H I})$ and find that $H\alpha/H\beta$ and $H\gamma/H\beta$ respectively decrease and increase with decreasing $N(\text{H I})$, but the effect is small, not exceeding 2–3 per cent. Therefore, departures from the case B cannot account for the observed hydrogen line ratios.

We use the emission line intensities (Table 2) and the direct T_e -method to derive the electron temperature and electron number density, and the ionic and total abundances of nitrogen, oxygen and neon in the interstellar medium of J1154+2443 as described in Izotov et al. (2006). As for magnesium, the determination of its abundance is described in Guseva et al. (2013).

The derived temperatures and element abundances are shown in Table 3. The oxygen abundances of J1154+2443 are 7.65 ± 0.01 with $C(H\beta) = 0.07$ and 7.62 ± 0.01 with $C(H\beta) = 0.25$, lower than the oxygen abundances $\sim 7.8 - 8.0$ derived in known low-redshift LyC leakers by Izotov et al. (2016a,b). The ratios of other element abundances to oxygen abundance are in the range obtained for dwarf emission-line galaxies (e.g. Izotov et al. 2006; Guseva et al. 2013).

Table 4. *HST*/COS observations

Name	Date	Exposure time (s)		
		(Central wavelength (Å))		
		MIRRORA	G140L	G160M
J1154+2443	2017-07-20	1408	8691 (1105)	5636 (1600)

4 *HST*/COS OBSERVATIONS AND DATA REDUCTION

The *HST*/COS (Green et al. 2012) observations of J1154+2443 were obtained in the course of the program GO14635 (PI: Y. I. Izotov). Some details of the observations are given in Table 4. The galaxy was first acquired using COS near ultraviolet (NUV) images with the MIRRORA setting. The galaxy region with the highest number of counts was automatically centered in the 2.5 arc-sec diameter spectroscopic aperture (Fig. 1a). Although the galaxy shows some structure with an extended low-surface-brightness (LSB) component, it is very compact and is localized in the central part of the spectroscopic aperture.

Spectra were obtained at COS Lifetime Position 3 with the gratings G140L and G160M, applying four focal-plane offset positions in each observation to minimize fixed-pattern noise and to patch grid-wire shadows and other detector blemishes. The G140L grating was used in the 1105 Å setup (wavelength range 1110–2150 Å, resolving power $R \approx 1400$ at 1150 Å), which includes the redshifted LyC emission. The G160M spectrum was obtained in the 1600 Å setup (wavelength range 1410–1773 Å, resolving power $R \approx 17000$ at 1600 Å) to resolve the redshifted Ly α $\lambda 1216$ Å line and study its profile.

The data were reduced with the CALCOS pipeline v2.21 adapted to handle spectra obtained at COS Lifetime Position 3, and custom software to improve the background subtraction and co-addition for faint targets (Worseck et al. 2016). We employed custom pulse height filtering to minimize the impact of detector dark current by measuring the range of pulse heights with physical flux in the spectral trace. For COS detector segment A we used pulse heights 1–12 containing > 99 per cent of the geocoronal Ly α flux. For segment B we estimated a pulse height range 3–15 from the spectral trace. For boxcar extraction we used 25 (27) pixel wide rectangular apertures for the G140L (G160M) spectra, preserving the spectrophotometry for compact sources while minimizing the background.

The detector dark current in the chosen aperture was estimated from dark monitoring exposures taken within ± 1 month of the science observations in similar ambient conditions (Worseck et al. 2016), and adopting the same pulse height cuts. We used the pulse height distribution to select dark exposures obtained in similar ambient conditions as the science data (see Appendix A for details). Low solar activity ensured that a sufficient number of dark exposures got selected, resulting in a negligible statistical error (≈ 2 per cent) of the dark current across the whole wavelength range of both gratings. Tests with dark exposures revealed that our dark subtraction procedure has negligible systematic error, and that the dark current can be modelled accurately with dark exposures with similar pulse height

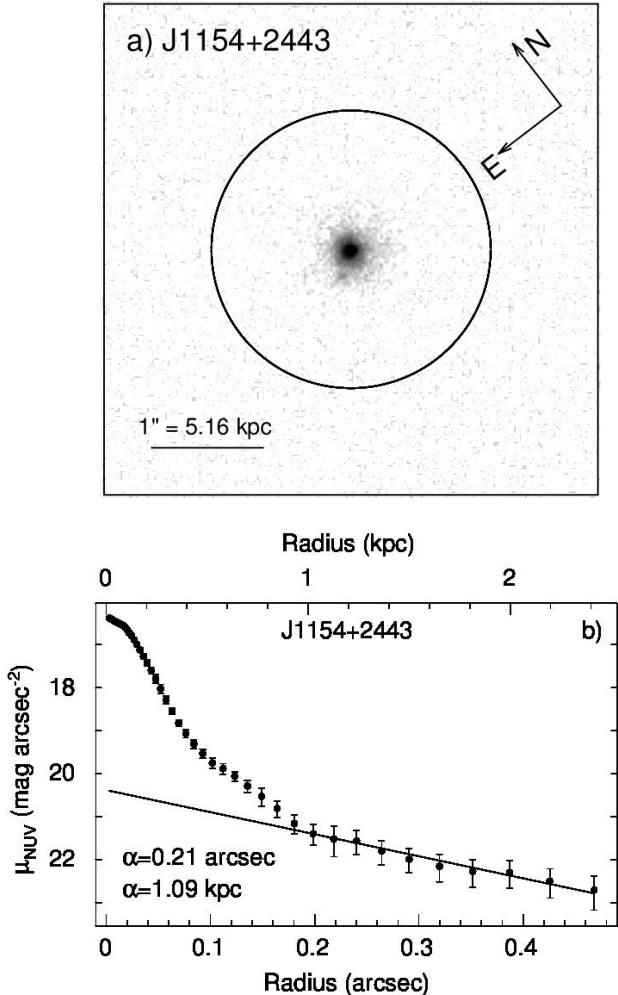


Figure 1. a) The *HST*/COS NUV acquisition image of J1154+2443 in log surface brightness scale. The COS spectroscopic aperture with a diameter of 2.5 arcsec is shown by a circle. The linear scale is derived adopting an angular size distance of 1064 Mpc. b) Surface brightness profile of J1154+2443 derived from the NUV acquisition image. The linear fit is shown for the range of radii used for fitting.

distributions but obtained at different orbit locations (Appendix A). The quasi-diffuse sky background was subtracted using the *GALEX* FUV map from Murthy (2014). Airglow contamination of N I 1200Å and O I 1304Å was eliminated by considering only data taken in orbital night in the affected wavelength ranges, while N I 1134Å and O I 1356Å line emission was negligible. For the G140L exposures we estimated and subtracted scattered geocoronal Ly α emission following Worseck et al. (2016).

We evaluated the accuracy of the estimated scattered light by comparing the fluxes obtained in the total exposure time (8691 s) and in orbital night (1797 s). In the LyC of the target the estimated total background error of 4–10 per cent does not significantly affect our analysis.

5 SURFACE BRIGHTNESS PROFILE IN THE NUV RANGE

We use the COS NUV acquisition image of J1154+2443 to determine its surface brightness (SB) profile. The galaxy is sufficiently compact with radius $\lesssim 0.5$ arcsec (Fig. 1a), therefore its image does not suffer from vignetting. The image of J1154+2443 was reduced to the absolute scale by using the total *GALEX* NUV magnitude (Table 1). Finally, the routine *ellipse* in *IRAF*²/*STSDAS*³ was used to produce the SB profile. The SB profile shown in Fig. 1b consists of two parts, one with a sharp SB increase in the central part, corresponding to the brightest star-forming region in the centre of the galaxy, and the second with a linear SB decrease (in magnitudes) of the extended low surface brightness component in the outward direction.

This linear decrease is characteristic of disc galaxies and can be described by the relation

$$\mu(r) = \mu(0) + 1.086 \times \frac{r}{\alpha}, \quad (1)$$

where μ is the surface brightness, r is the distance from the centre, and α is the disc scale length of the outer disc.

The derived scale length $\alpha = 1.09$ kpc (Fig. 1b) is very similar to scale lengths of other LyC leakers (Izotov et al. 2016b). The corresponding surface density of star formation rate $\Sigma = \text{SFR}/(\pi\alpha^2)$ is $5.1 M_{\odot} \text{ yr}^{-1} \text{ kpc}^{-2}$. The size of J1154+2443 in the UV can be directly compared with those of galaxies at high redshifts. Curtis-Lake et al. (2016), Paulino-Afonso et al. (2017) and Bouwens et al. (2017) have shown that half-light radii of $z = 2 - 8$ galaxies are $\sim 0.1 - 1$ kpc, which are similar to the J1154+2443 half-light radius of ~ 0.2 kpc (Fig. 1b). Adopting the latter value we obtain much higher Σ of $\sim 150 M_{\odot} \text{ yr}^{-1} \text{ kpc}^{-2}$ which together with the SFR is a characteristic of the central part of the galaxy.

6 INTEGRATED CHARACTERISTICS OF J1154+2443

Using SDSS and *GALEX* photometric and spectroscopic data, we derive in this Section integrated characteristics of J1154+2443 such as luminosities and absolute magnitudes, SFR and stellar mass M_{\star} .

6.1 Absolute magnitudes and the H β luminosity

The observed fluxes were transformed to absolute magnitudes and luminosities adopting a luminosity distance derived with a cosmological calculator (NED, Wright 2006), based on the cosmological parameters $H_0 = 67.1 \text{ km s}^{-1} \text{ Mpc}^{-1}$, $\Omega_{\Lambda} = 0.682$, $\Omega_m = 0.318$ (Ade et al. 2014). We derived an extinction-corrected absolute SDSS AB g -band magnitude $M_g = -20.00$ mag and a *GALEX* FUV magnitude $M_{FUV} = -20.12$ mag adopting $C(H\beta) = 0.07$ (Table

² *IRAF* is distributed by the National Optical Astronomy Observatories, which are operated by the Association of Universities for Research in Astronomy, Inc., under cooperative agreement with the National Science Foundation.

³ *STSDAS* is a product of the Space Telescope Science Institute, which is operated by AURA for NASA.

Table 5. Integrated parameters

Name	$12+\log O/H^a$	D^b (Mpc)	M_g^a (mag)	M_{FUV}^a (mag)	$\log M_\star^{a,c}$ ($\log M_\odot$)	SB age ^a (Myr)	SFR ^a ($M_\odot \text{ yr}^{-1}$)	α^d (kpc)
J1154+2443	7.65 ± 0.01	2064	-20.00	-20.12	8.20	2.6	18.9	1.09

^aThe internal extinction coefficient $C(H\beta) = 0.07$ is adopted.

^bLuminosity distance.

^c M_\star is the total mass of the young and old stellar populations.

^dExponential disc scale length.

5). These magnitudes are 0.5 – 1.0 mag fainter than the respective values of the five LyC leakers studied by Izotov et al. (2016a,b). This is expected because of the luminosity-metallicity relation for compact SFGs (Izotov et al. 2015), J1154+2443 having a lower metallicity compared to other LyC leakers.

The $H\beta$ luminosity $L(H\beta)$ and SFR were obtained from the extinction-corrected $H\beta$ flux with $C(H\beta) = 0.07$. For J1154+2443 we derived $L(H\beta) = 4.6 \times 10^{41} \text{ erg s}^{-1}$. The SFR = $10.2 M_\odot \text{ yr}^{-1}$ is determined from $L(H\beta)$ using the relation by Kennicutt (1998). It should be increased by a factor $1/[1-f_{\text{esc}}(\text{LyC})]$ equal to 1.85, to take into account the escaping ionizing radiation (see Sect. 8). This gives SFR = $18.9 M_\odot \text{ yr}^{-1}$. It is at the low end of the SFR range 14 – 50 $M_\odot \text{ yr}^{-1}$ derived by Izotov et al. (2016a,b) for the five LyC leakers with higher metallicities and absolute brightnesses. However, its specific star formation rate $\text{sSFR} = \text{SFR}/M_\star = 1.2 \times 10^{-7} \text{ yr}^{-1}$ is the second highest in the sample.

6.2 Stellar mass

The stellar mass of J1154+2443 is derived from fitting the spectral energy distribution (SED) of the continuum in its SDSS spectrum in the wavelength range 3600–10300 Å. We generally use the fitting method described e.g. in Izotov et al. (2016b). In J1154+2443, with a rest-frame $H\beta$ equivalent width $\text{EW}(H\beta) \sim 160 \text{ \AA}$, nebular continuum is strong and should be accounted for in SED modelling. We note that the photometric data and UV spectra were not used in the SED fitting, but they are useful for checking the consistency of the SEDs derived from the optical spectra.

To fit the SEDs we carried out a series of Monte Carlo simulations. A grid of instantaneous burst SEDs with a wide range of ages from 0 Myr to 15 Gyr was calculated with STARBURST99 (Leitherer et al. 1999, 2014) to derive the SED of the galaxy stellar component. Input parameters for the grid calculations included Padova stellar evolution tracks (Girardi et al. 2000), models of stellar atmospheres by Lejeune, Buser & Cuisiner (1997) and Schmutz, Leitherer & Gruenwald (1992), and the stellar initial mass function of Salpeter (1955) with the upper and low stellar mass limits of $100 M_\odot$ and $0.1 M_\odot$, respectively. Then the stellar SED with any star-formation history can be obtained by integrating the instantaneous burst SEDs over time with a specified time-varying SFR. Given the electron temperature T_e in the H II region, we interpolated emissivities by Aller (1984) for the nebular continuum in the T_e range of 5000 – 20000 K. Then the nebular continuum luminosity at any wavelength is derived from the observed $H\beta$ luminosity. The fraction of the nebular continuum in the total continuum near $H\beta$ is de-

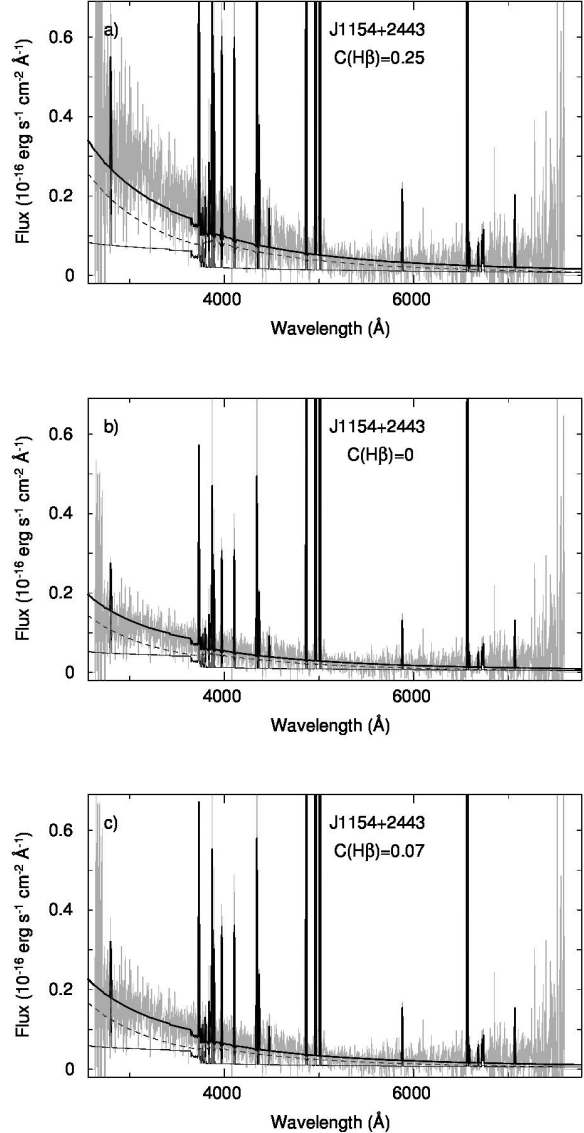


Figure 2. SED fitting of the J1154+2443 optical spectrum. The rest-frame extinction-corrected SDSS spectrum is shown by the grey line. The stellar, ionized gas, and total modelled SEDs are shown by dashed, thin solid and thick solid lines, respectively. **a)** The case with the internal extinction $C(H\beta) = 0.25$ derived including $H\alpha$ emission line. **b)** The case with $C(H\beta) = 0$. **c)** The case with $C(H\beta) = 0.07$ derived excluding $H\alpha$ emission line.

terminated by the ratio of the observed $\text{EW}(\text{H}\beta)$ to the value of $\sim 1000\text{\AA}$ for the pure nebular emission. The emission lines with fluxes measured in the SDSS spectrum were added to the total continuum.

The star-formation history is approximated assuming a short burst with age $t_y < 10$ Myr and a continuous star formation for the older population with a constant SFR during the time interval between t_i and t_f ($t_f < t_i$ and zero age is now). The contribution of each stellar population to the SED was parameterized by the ratio $b = M_y/M_o$, where M_y and M_o are the masses of the young and old stellar populations formed during the recent burst and the prior continuous star formation, respectively.

We calculated 10^5 Monte Carlo models to derive the stellar SED by randomly varying t_y , t_i , t_f , and b , while the fraction of the nebular continuum is determined by the ratio of the observed $\text{EW}(\text{H}\beta)$ to $\sim 1000\text{\AA}$. We also calculate the equivalent widths $\text{EW}(\text{H}\beta)$ and $\text{EW}(\text{H}\alpha)$ for each model, integrating over the time luminosities of emission lines and adjacent continua. The best solution is required to fulfill the following conditions. First, only models, in which both $\text{EW}(\text{H}\beta)$ and $\text{EW}(\text{H}\alpha)$ are in agreement with the observed values within 5 per cent, were selected. Second, the best modelled SED satisfying first two conditions was found from χ^2 minimization of the deviation between the modelled and the observed continuum.

We find from the best SED fit that the stellar mass $M_\star = 10^{8.20} M_\odot$ of J1154+2443. It is at the low end of the M_\star range $10^{8.22} - 10^{9.59} M_\odot$ for other confirmed low-redshift LyC leakers (Izotov et al. 2016a,b), and is typical to the mass of dwarf galaxies.

As for the starburst age t_y , we note that it is mainly dependent on the $\text{H}\beta$ and $\text{H}\alpha$ equivalent widths and is higher for lower $\text{EW}(\text{H}\beta)$ and $\text{EW}(\text{H}\alpha)$. The presence of escaping ionizing radiation complicates the determination of the starburst age, because this radiation does not produce $\text{H}\beta$ and $\text{H}\alpha$ emission. Therefore, $\text{EW}(\text{H}\beta)$ and $\text{EW}(\text{H}\alpha)$ are reduced in the case of large $f_{\text{esc}}(\text{LyC})$, resulting in an overestimation of the starburst age. To overcome this problem in the case of J1154+2443, during the SED fitting procedure, we have derived iteratively $f_{\text{esc}}(\text{LyC})$ until its value converges. We start by adopting an initial $f_{\text{esc}}(\text{LyC})$ and deriving the best-fit SED by randomly varying t_y , t_i , t_f , and b . This model should also reproduce the observed $\text{EW}(\text{H}\beta)$ and $\text{EW}(\text{H}\alpha)$. A new iterated value of $f_{\text{esc}}(\text{LyC})$ is then derived as the ratio of the observed LyC flux density to its intrinsic value as determined from the best-fit SED. Then the determination of the best-fit SED is repeated with the new $f_{\text{esc}}(\text{LyC})$. Only a few iterations are needed for $f_{\text{esc}}(\text{LyC})$ to converge, regardless of its initial value. This iteration procedure adopting $C(\text{H}\beta) = 0.07$ results in a starburst age $t_y = 2.6$ Myr instead of 3.3 Myr, the value corresponding to $f_{\text{esc}}(\text{LyC}) = 0$. The determination of $f_{\text{esc}}(\text{LyC})$ is further described in Sect. 8.

The optical galaxy spectra with the overlaid stellar (dashed line), nebular (thin solid line) and total stellar and nebular (thick solid line) best-fit SEDs are shown in Fig. 2 for $R(V) = 3.1$ and three values of the internal extinction $C(\text{H}\beta)$, 0.25 (Fig. 2a), 0 (Fig. 2b), and 0.07 (Fig. 2c). It is seen that the observed spectrum shortward $\sim 3600\text{\AA}$ is not reproduced by the modelled SED if $C(\text{H}\beta) = 0.25$ is adopted (Fig. 2a). It is better reproduced by the modelled

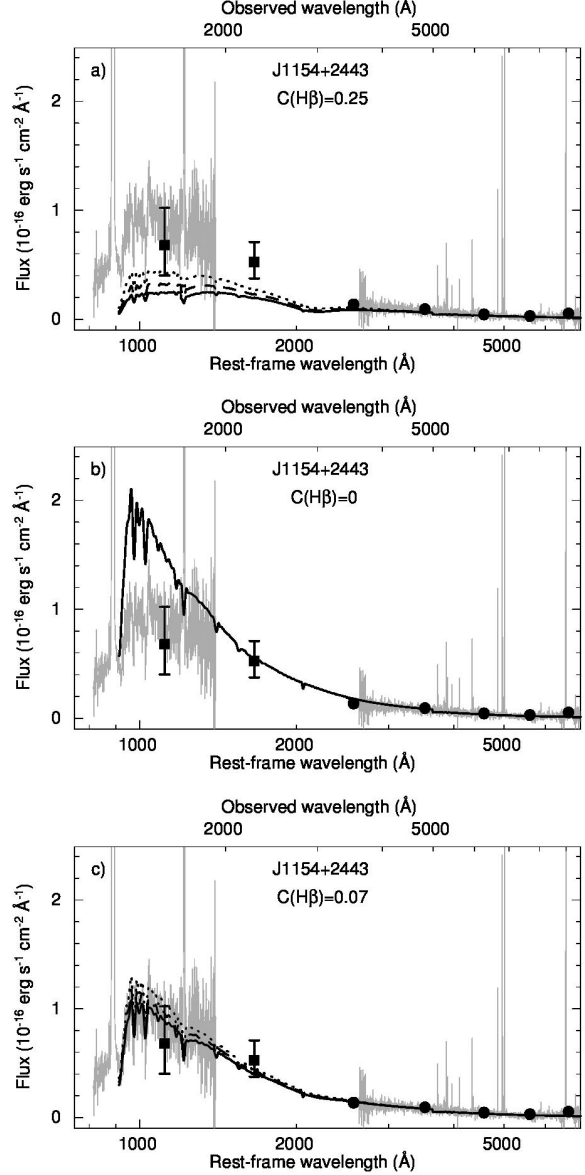


Figure 3. A comparison of the observed UV and optical spectra, and photometric data with the modelled SEDs. The observed spectrum of J1154+2443 is shown by grey line. The total GALEX and SDSS photometric fluxes are represented by filled squares and filled circles, respectively. Modelled SEDs, which are reddened by the Milky Way extinction with $R(V)_{\text{MW}} = 3.1$ and internal extinction with $R(V)_{\text{int}} = 3.1, 2.7,$ and 2.4 adopting the reddening law by Cardelli et al. (1989) are shown by dotted, dashed and solid lines, respectively. **a)** The case with the internal extinction $C(\text{H}\beta) = 0.25$ derived including $\text{H}\alpha$ emission line. **b)** The case with $C(\text{H}\beta) = 0$. **c)** The case with $C(\text{H}\beta) = 0.07$ derived excluding $\text{H}\alpha$ emission line.

SED adopting zero internal extinction (Fig. 2b), but the best agreement is found if $C(\text{H}\beta) = 0.07$ is adopted (Fig. 2c). This conclusion is not changed if we adopt $R(V) = 2.4$ or 2.7 . The stellar mass and starburst age derived from our fitting of the SDSS optical spectrum with $C(\text{H}\beta) = 0.07$ and $R(V) = 3.1$ are presented in Table 5.

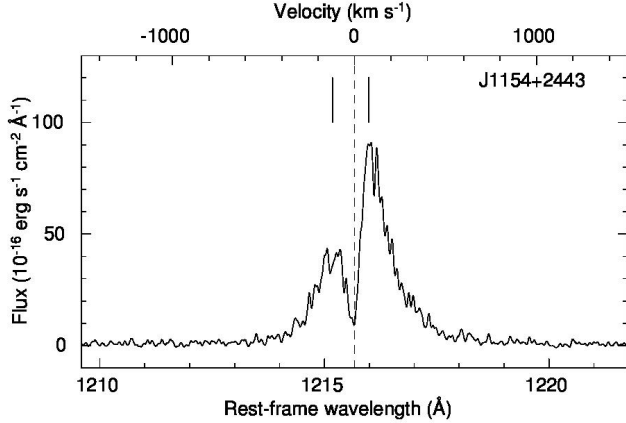


Figure 4. The Ly α profile of J1154+2443. The centre of the line is indicated by a vertical dashed line. The locations of the blue and red peaks are shown by short solid vertical lines.

6.3 Reddening law in the UV range

We use the extrapolation to the UV range of the SED derived from the optical SDSS spectrum. This is needed to verify what reddening law and internal extinction coefficient $C(H\beta)$ are most appropriate in the UV range of J1154+2443 in order to correct for extinction observed fluxes in this range. Izotov et al. (2016a,b), using the same approach, have shown that the correction for extinction in the optical range for LyC leakers is insensitive to variations of $R(V)$ because of low extinction. On the other hand they found that the observed spectra of the LyC leakers in the entire UV + optical spectra are best fitted with the reddening law by Cardelli et al. (1989) adopting $R(V)_{\text{int}} = 2.4 - 2.7$, steeper than the canonical curve with $R(V) = 3.1$, and resulting in a larger UV extinction correction.

The observed UV *HST*/COS and optical SDSS spectra of J1154+2443 are shown in Fig. 3 by grey lines. Their fluxes are consistent within the errors with the SDSS and *GALEX* photometric fluxes for the entire galaxy shown by the filled circles and filled squares, respectively. The consistency between the spectroscopic and photometric data in the optical range implies that almost all the galaxy emission is inside the spectroscopic aperture, and thus aperture corrections are not needed.

To compare with the observed spectrum, we reddened the intrinsic modelled SEDs in the optical range and their extrapolations in the UV range for three values of the internal extinction coefficient $C(H\beta)$, 0.25 (Fig. 3a), 0 (Fig. 3b) and 0.07 (Fig. 3c), adopting $R(V)_{\text{MW}} = 3.1$ for the Milky Way extinction, and $R(V)_{\text{int}} = 3.1$ (dotted line), 2.7 (dashed line) and 2.4 (solid line) for the internal extinction. The Milky Way extinction was applied to the SED redshifted to the observed wavelengths and the internal extinction to the spectrum at rest-frame wavelengths. We adopted the reddening curve by Cardelli et al. (1989) parameterized by the $R(V)_{\text{MW}}$ and $R(V)_{\text{int}}$, except for $\lambda \leq 1250$ Å, where the reddening curve of Mathis (1990) with the respective $R(V)$'s is used.

It is seen in Figs. 3a and 3b that the modelled SEDs with $C(H\beta) = 0.25$ and 0 fail to reproduce the observed UV spectrum regardless of the $R(V)$ value, while the agreement

is good with $C(H\beta) = 0.07$ (Fig. 3c). Therefore, in the subsequent analysis, we will adopt the latter value of $C(H\beta)$, derived from the observed Balmer decrement excluding the $H\alpha$ emission line. We find that the observed UV spectrum of J1154+2443 in Fig. 3c is best fitted by the SED reddened with $R(V)_{\text{int}} = 2.4$, in close agreement with conclusions made by Izotov et al. (2016a,b) for five LyC leakers, while the SEDs reddened with higher $R(V)_{\text{int}}$ lie above the observed UV spectrum, requiring a higher extinction in the UV range than that derived from the Balmer decrement. Izotov et al. (2016a,b) also considered reddening laws by Calzetti, Kinney & Storchi-Bergmann (1994) and Calzetti et al. (2000) and found that the SEDs reddened with this law do not fit the observed UV spectra of LyC leakers, requiring a higher extinction in the UV range than that by Cardelli et al. (1989) with $R(V)_{\text{int}} = 3.1$. For subsequent discussion of the J1154+2443 UV spectrum, we adopt $R(V)_{\text{int}} = 2.4$.

7 LY α EMISSION

Strong Ly α $\lambda 1216$ Å emission-line is detected in the medium-resolution spectrum of J1154+2443 (Fig. 4). The profile shows two peaks at -121 km s $^{-1}$ and $+78$ km s $^{-1}$, labelled by two short vertical lines in the Figure. While the shape of the Ly α profile in J1154+2443 is similar to that observed in known LyC leakers (Verhamme et al. 2017) and in some other GP galaxies (Jaskot & Oey 2014; Henry et al. 2015; Yang et al. 2017), the separation between the blue and red peaks of 199 km s $^{-1}$ is the lowest among all low-redshift LyC leakers and other GP galaxies observed so far with the *HST*/COS. According to the radiation transfer models of Verhamme et al. (2015), such a low separation indicates a very low column density of the neutral gas in J1154+2443 and thus a high escape fraction of the Ly α emission. We find that the rest-frame equivalent width $\text{EW}(\text{Ly}\alpha)$ of the Ly α line equal to 133 Å and the extinction-corrected luminosity $L(\text{Ly}\alpha)$ (Table 6) are among the highest for the low-redshift LyC leakers (Izotov et al. 2016a,b).

Comparing the extinction-corrected Ly α /H β flux ratio of 31.3 (Table 6) and the case B flux ratio of 31.9 obtained with the *CLOUDY* code (Ferland et al. 1998, 2013) for an electron temperature $T_e = 18300$ K and an electron number density $N_e = 1000$ cm $^{-3}$, we find that the Ly α escape fraction is $f_{\text{esc}}(\text{Ly}\alpha) = 98$ per cent, the highest known so far for LyC leakers and other GP galaxies (Henry et al. 2015; Izotov et al. 2016a,b; Yang et al. 2017).

8 ESCAPING LYMAN CONTINUUM RADIATION

Our primary aim in this paper is to examine the COS spectrum of J1154+2443 obtained with the G140L grating and to derive the escape fraction of ionizing radiation.

8.1 Low-resolution G140L spectrum of J1154+2443

The observed G140L spectrum with a total exposure of 8691 s is shown in Fig. 5a together with the predicted intrinsic SED obtained from fitting the observed optical SDSS

Table 6. Parameters for the H β and Ly α emission lines

Name	$A(V)_{\text{MW}}^{\text{a}}$	$A(V)_{\text{int}}^{\text{a}}$	$A(\text{Ly}\alpha)^{\text{a}}$	F^{b}	H β EW ^c	L^{d}	F^{b}	Ly α EW ^c	L^{d}	Ly α /H β^{e}	case B ^f	$f_{\text{esc}}(\text{Ly}\alpha)$
J1154+2443	0.049	0.145	0.694	7.3	160	0.46	148.9	133	14.38	31.3	31.9	0.98

^aExtinction in mags. $A(\text{Ly}\alpha) = A(\text{Ly}\alpha)_{\text{MW}} + A(\text{Ly}\alpha)_{\text{int}}$, where $A(\text{Ly}\alpha)_{\text{MW}}$ is derived for $\lambda=1216 \times (1+z)\text{\AA}$ and $R(V)=3.1$, and $A(\text{Ly}\alpha)_{\text{int}}$ is derived for $\lambda=1216\text{\AA}$ and $R(V)=2.4$.

^bObserved flux density in $10^{-16} \text{ erg s}^{-1} \text{ cm}^{-2}$.

^cRest-frame equivalent width in \AA .

^dLuminosity in $10^{42} \text{ erg s}^{-1}$.

^eExtinction-corrected flux ratio.

^fCase B Ly α /H β flux ratio.

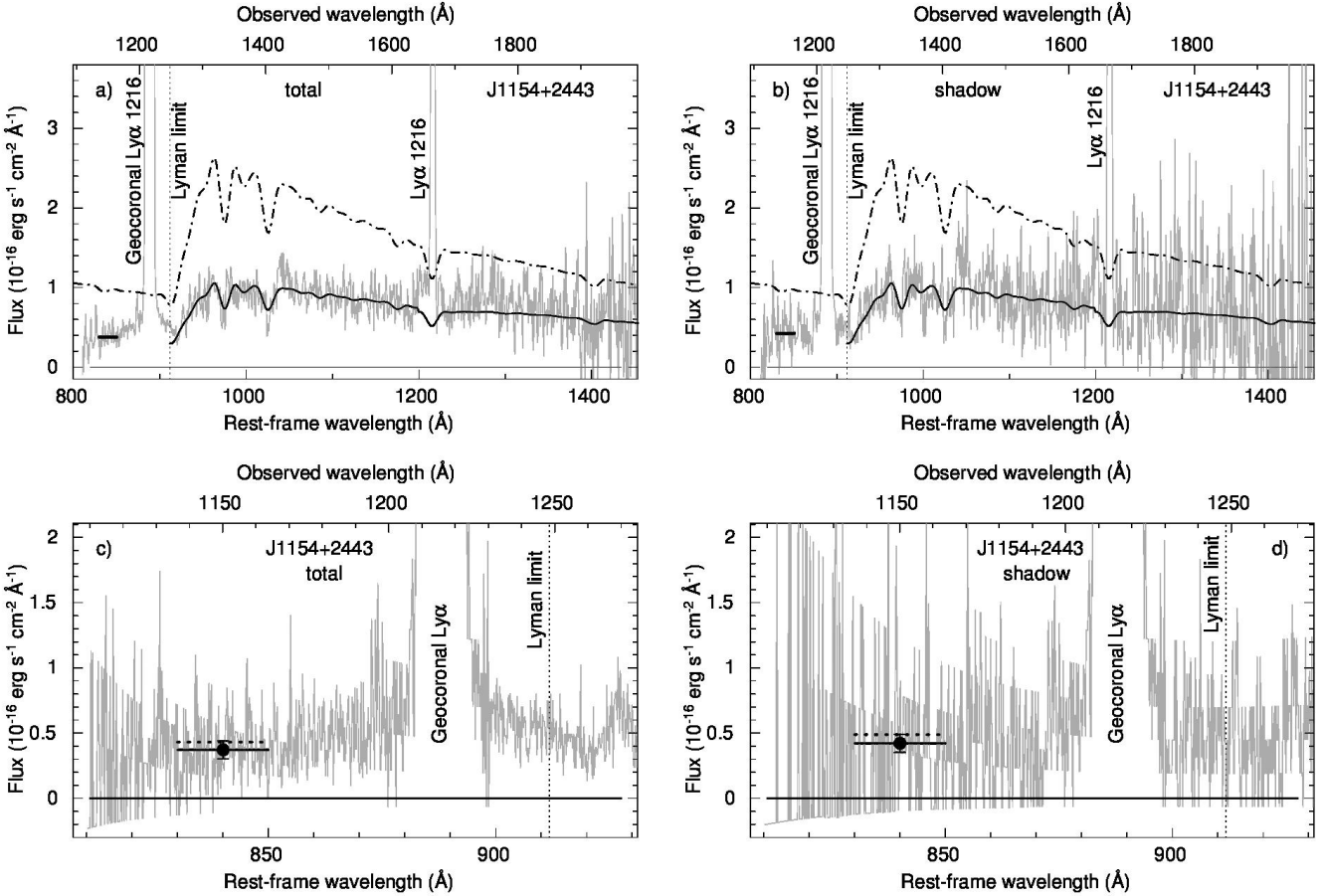


Figure 5. a) COS G140L spectrum of J1154+2443 obtained with an exposure of 8691 s and smoothed by 12-pixel binning. On top of the observed spectrum (grey line) is superposed the modelled SED, reddened by both the Milky Way and internal extinctions (solid line). The unreddened intrinsic SED is shown by the dash-dotted line. The thick and short solid horizontal line at the rest-frame $\lambda = 830 - 850\text{\AA}$ shows the level of the observed LyC flux density. Zero flux is represented by a black solid horizontal line while the Lyman limit is indicated by the vertical dotted line. b) Same as in a) but the spectrum is taken only in orbital shadow with an exposure time of 1797 s. c) Expanded COS spectrum with the total exposure time of 8691 s showing the Lyman continuum. The spectrum is smoothed by 3-pixel binning. The average value of the observed LyC flux density with the 3σ error bar is shown by the filled circle. The solid horizontal line indicates the observed mean LyC flux density and the wavelength range of $830 - 850\text{\AA}$ used for averaging, while the dotted horizontal line represents the LyC level after correction for the Milky Way extinction. Zero flux is also shown by a horizontal line. d) Same as in c) but the spectrum taken in orbital shadow is shown.

spectrum (see Section 6). The strong line at the observed wavelength of 1216\AA is the residual of the geocoronal Ly α emission, while the second brightest line labelled “Ly α 1216” is the Ly α line of the galaxy. It is seen that the flux short-

ward the Lyman limit at the rest-frame wavelength 912\AA indicated by a dotted vertical line is far above the zero level.

There is a slight increase of the flux in the rest-frame wavelength range $855 - 912\text{\AA}$ centered at the geocoronal Ly α emission line. The first suggestion is that this increase is due

Table 7. LyC escape fraction

Name	Monochromatic flux density ^a			LyC escape fraction	
	$I_{\text{obs}}(840)^{\text{b}}$	$I_{\text{esc}}(840)^{\text{c}}$	$I_{\text{mod}}(840)^{\text{d}}$	$f_{\text{esc}}^{\text{e}}$	$f_{\text{esc}}^{\text{f}}$
J1154+2443	3.8±0.2	4.4±0.2	9.6	0.46±0.02	0.47

^ain 10^{-17} erg s⁻¹ cm⁻² Å⁻¹.

^bObserved flux density in the wavelength range 830 – 850 Å.

^cFlux density corrected for the Milky Way extinction.

^dIntrinsic flux density derived from the modelled SED.

^e $I_{\text{esc}}/I_{\text{mod}}(840)$ (first method, Eq. 2).

^f $I_{\text{esc}}/I_{\text{mod}}(840)$ (second method, Eqs. 3 and 4).

to the geocoronal Ly α scattered light. However, we argued in Section 4 that the scattered light might be not significant. To validate this point we use the COS spectrum of a quasar at $z = 3.9$ that shows highly saturated He II absorption with the rest-frame wavelength of ~ 240 Å and therefore with a very little source flux which is redshifted to the wavelength range near the geocoronal Ly α line. In this case, almost all emission would be attributed to the scattered geocoronal Ly α emission line. However, we find that geocoronal flux is small at $\lambda > 1230$ Å and at 1180 – 1200 Å. This indirect test shows that the scattered geocoronal Ly α emission is insufficient to explain the flux increase around the geocoronal Ly α emission line.

To further explore whether scattered geocoronal Ly α emission is important, we compare in Fig. 5b the spectrum during orbital shadow with an exposure 1797 s when the flux of the geocoronal line is decreased by a factor of ~ 20 with respect to the total spectrum (Fig. 5a). It is seen that the presence of the flux increase around the geocoronal Ly α line is not so evident, although we cannot totally exclude the contribution of the scattered geocoronal Ly α light in the case of J1154+2443. However, the signal-to-noise ratio in Fig. 5b is not sufficient to make more definite conclusions. Therefore, to be safe, we exclude the wavelength range 855 – 912 Å and use the range 830 – 850 Å (corresponding to the observed wavelength range 1136 – 1164 Å) for the LyC flux determination. The average flux density at these wavelengths, attributed to the escaping LyC emission of J1154+2443, is indicated in Figs. 5a and 5b by the short horizontal solid lines.

This is illustrated more clearly in Figs. 5c and 5d, which show a blow-up of the LyC spectral region. With the flux density of $(3.8 \pm 0.2) \times 10^{-17}$ erg s⁻¹ cm⁻² Å⁻¹ averaged over the rest-frame spectral range 830 – 850 Å, the Lyman continuum is detected at the $\sim 18\sigma$ level in the total exposure spectrum.

The observed LyC emission should be corrected for extinction from the Milky Way before the determination of the LyC escape fraction. The average LyC flux densities of 4.4×10^{-17} erg s⁻¹ cm⁻² Å⁻¹ and 4.8×10^{-17} erg s⁻¹ cm⁻² Å⁻¹, corrected for the Milky Way extinction, are shown respectively in Figs. 5c and 5d by the dotted horizontal lines. The observed and corrected flux densities derived from the total exposure which we adopt, are reported in Table 7.

8.2 LyC escape fraction of J1154+2443

To derive the escape fraction of Lyman continuum photons, $f_{\text{esc}}(\text{LyC})$, Izotov et al. (2016a,b) used the modelled flux density $I_{\text{mod}}(900)$ of the Lyman continuum emission at 900 Å and compared it to the observed flux density (after correction for extinction in the Milky Way). They proposed two methods to derive $I_{\text{mod}}(900)$. The first method is based on the SED fit to the observed SDSS spectrum in the optical range described in Sect. 6. The extrapolation of this fit predicts the UV emission, including the Lyman continuum. The modelled UV flux densities $I_{\text{mod}}(\lambda)$ are shown by the dash-dotted line in Fig. 5a. The reddened modelled UV SED is represented by the solid line. This SED is the same as the SED shown by the solid line in Figs. 2 – 3 for $R(V)_{\text{MW}} = 3.1$, $A(V)_{\text{MW}} = 0.049$ mag from the NED, $A(V)_{\text{int}} = 0.145$ mag as derived from the Balmer decrement, and $R(V) = 2.4$ (see details in Sect. 6). It is seen that the reddened SED reproduces very well the observed spectrum (grey line) for rest-frame wavelengths > 912 Å.

The second method of the I_{mod} determination uses the fact that the intensities of hydrogen recombination lines are approximately proportional to the number of ionizing photons emitted per unit time, $N(\text{LyC})$.

Both methods use the extinction-corrected flux density $I(\text{H}\beta)$ and rest-frame equivalent width $\text{EW}(\text{H}\beta)$ of the H β emission line, both derived from observations. Since the observed LyC flux density is measured in the wavelength range 830 – 850 Å, because the flux density at 900 Å might be affected by geocoronal Ly α emission, we adopt $\lambda = 840$ Å. Then the escape fraction $f_{\text{esc}}(\text{LyC})$ is derived from

$$f_{\text{esc}}(\text{LyC}) = \frac{I_{\text{esc}}(840)}{I_{\text{mod}}(840)}. \quad (2)$$

Using Eq. 2 we derive the very high escape fraction $f_{\text{esc}}(\text{LyC}) = 46 \pm 2$ per cent accounting for the uncertainty of the observed monochromatic flux density.

For the second method Izotov et al. (2016b) considered the relation between the modelled flux densities of the H β emission line $I(\text{H}\beta)$ and the intrinsic monochromatic flux density $I_{\text{mod}}(900)$. The advantage of the second method is that there is no need to fit the SED. The $I(\text{H}\beta)$ is proportional to $[1 - f_{\text{esc}}(\text{LyC})]N(\text{LyC})$, where $N(\text{LyC})$ is the production rate of ionizing photons in the entire LyC wavelength range. The shape of the ionizing spectrum depends on starburst age. Therefore, the $I_{\text{mod}}(900)/N(\text{LyC})$ ratio and correspondingly the $I(\text{H}\beta)/I_{\text{mod}}(900)$ ratio are not constant and also depend on starburst age. However, Izotov et al. (2016b) have shown that, in the case of a small $f_{\text{esc}}(\text{LyC})$,

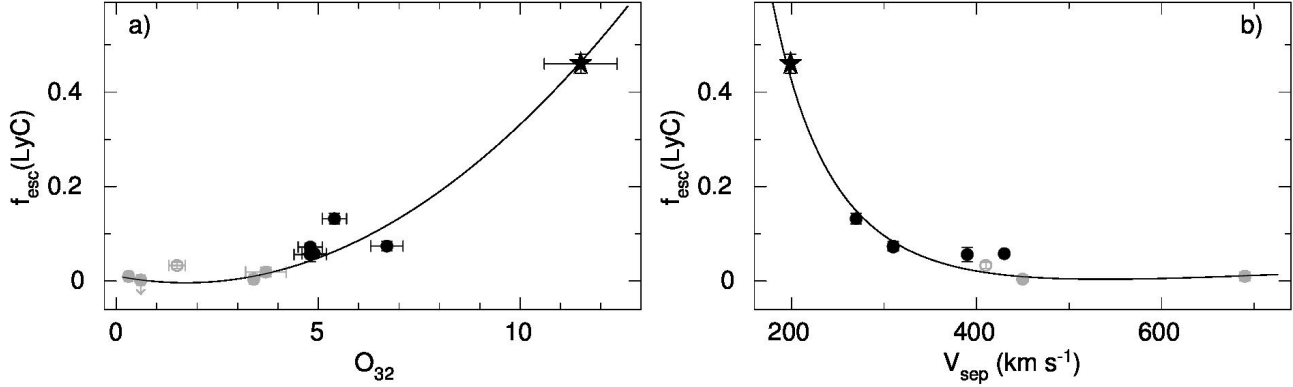


Figure 6. **a)** Relation between the Lyman continuum escape fraction $f_{\text{esc}}(\text{LyC})$ and the $\text{O}_{32} = [\text{O III}]\lambda 5007/[\text{O II}]\lambda 3727$ emission-line ratio for low-redshift LyC leaking galaxies observed with the *FUSE* (open circle) and *HST/COS* (filled symbols). Compact SFGs from Izotov et al. (2016a,b) are shown by black filled circles. The galaxy from Borthakur et al. (2014) and the galaxies from Leitherer et al. (2016) with $f_{\text{esc}}(\text{LyC})$ derived by Chisholm et al. (2017) are represented by grey filled circles. Haro 11 (Leitet et al. 2013) and J1154+2443 are shown by the open circle and filled star, respectively. **b)** Relation between $f_{\text{esc}}(\text{LyC})$ and a separation V_{sep} between the blue and red peaks of the Ly α emission line for low-redshift LyC leaking galaxies observed with the *FUSE* and *HST/COS*. V_{sep} for J1154+2443 is from this paper and for other galaxies are from Verhamme et al. (2017). Symbols are the same as in **a)**. Solid lines in both panels are most likelihood regressions.

the latter ratio can be fairly accurately constrained using a relation between the $I(\text{H}\beta)/I_{\text{mod}}(900)$ ratio and $\text{EW}(\text{H}\beta)$, since both the $\text{H}\beta$ flux density and the $\text{H}\beta$ equivalent width can directly be derived from observations. We have modified eq. 4 in Izotov et al. (2016b) for the case of a large $f_{\text{esc}}(\text{LyC})$, adopting $\lambda = 840\text{\AA}$ instead of 900\AA and STARBURST99 instantaneous burst models (Leitherer et al. 1999) for the J1154+2443 metallicity:

$$A = \frac{I(\text{H}\beta)}{I_{\text{mod}}(840)} = 3.47 \times \left[\frac{\text{EW}(\text{H}\beta)}{1 - f_{\text{esc}}(\text{LyC})} \right]^{0.181}, \quad (3)$$

where $\text{EW}(\text{H}\beta)$ is the rest-frame $\text{H}\beta$ equivalent width in \AA . We finally obtain

$$f_{\text{esc}}(\text{LyC}) = \frac{I_{\text{esc}}(840)}{I_{\text{mod}}(840)} = A \frac{I_{\text{esc}}(840)}{I(\text{H}\beta)}. \quad (4)$$

The escape fraction $f_{\text{esc}}(\text{LyC})$ obtained with the second method, derived iteratively from Eqs. 3 and 4 with adopted $I_{\text{esc}}(840) = 4.4 \times 10^{-17} \text{ erg s}^{-1} \text{ cm}^{-2} \text{ \AA}^{-1}$ and $I(\text{H}\beta) = 9.1 \times 10^{-16} \text{ erg s}^{-1} \text{ cm}^{-2}$ is 47 per cent, in excellent agreement with the first method. As in the case of the first method, only a few iterations are needed for $f_{\text{esc}}(\text{LyC})$ to converge in the second method.

Thus, we find that the LyC escape fraction in J1154+2443 with $\text{O}_{32} = 11.5$ is considerably higher than the escape fractions in all known low-redshift LyC leakers with lower O_{32} (Leitet et al. 2013; Borthakur et al. 2014; Leitherer et al. 2016; Izotov et al. 2016a,b).

8.3 Dependences of $f_{\text{esc}}(\text{LyC})$ on O_{32} and V_{sep}

In Fig. 6a we present the relation between $f_{\text{esc}}(\text{LyC})$ and O_{32} for known low-redshift LyC leaking galaxies. It shows a relatively tight trend of increasing $f_{\text{esc}}(\text{LyC})$ with increasing O_{32} , described by the regression relation

$$f_{\text{esc}}(\text{LyC}) = 4.88 \times 10^{-3} \text{O}_{32}^2 - 1.67 \times 10^{-2} \text{O}_{32} + 1.07 \times 10^{-2}. \quad (5)$$

The relation described by Eq. 5 shows that compact low-mass SFGs with high O_{32} ratios may lose a considerable

fraction of their LyC emission to the IGM. Thus, we confirm and extend the correlation between $f_{\text{esc}}(\text{LyC})$ and O_{32} first found by Izotov et al. (2016b) and later considered by Faisst (2016).

For comparison, currently the most robust high-redshift Lyman continuum leaking galaxy is *Ion2* at $z = 3.2$ with a relative escape fraction of $0.64_{-0.1}^{+1.1}$ (Vanzella et al. 2015; de Barros et al. 2016). This galaxy shares many properties with the low-redshift LyC leakers (cf. Schaerer et al. 2016). In particular, *Ion2* is characterized by a high ratio $\text{O}_{32} > 10$, in line with the selection criterion used in this paper and by Izotov et al. (2016a,b).

In Fig. 6b we show the tight dependence of $f_{\text{esc}}(\text{LyC})$ on the separation V_{sep} between the blue and red peaks of the Ly α emission line in LyC leakers. The regression line to this dependence is

$$f_{\text{esc}}(\text{LyC}) = \frac{4.28 \times 10^4}{V_{\text{sep}}^2} - \frac{1.59 \times 10^2}{V_{\text{sep}}} + 0.15, \quad (6)$$

where V_{sep} is expressed in km s^{-1} .

We note that the correlation between $f_{\text{esc}}(\text{LyC})$ and V_{sep} (Fig. 6b) is tighter than that between $f_{\text{esc}}(\text{LyC})$ and O_{32} . Physically this may be because both LyC and Ly α escaping radiation are determined by the column density of the neutral gas in LyC leaking galaxies and by the velocity field in the case of Ly α radiation (e.g. Verhamme et al. 2015, 2017). On the other hand, O_{32} depends on several other parameters such as metallicity and ionization parameter, in addition to the column density of the neutral gas (Jaskot & Oey 2013; Nakajima & Ouchi 2014; Stasińska et al. 2015; Izotov et al. 2017). The relation described by Eq. 6 might be important for the construction of radiative transfer models which simultaneously reproduce $f_{\text{esc}}(\text{LyC})$ and the Ly α profile. Similar relations for a smaller sample, with a lower range of $f_{\text{esc}}(\text{LyC})$ and V_{sep} , was discussed by Verhamme et al. (2017). The high $f_{\text{esc}}(\text{LyC})$ and low V_{sep} for J1154+2443 are indicative of a very low neutral gas column density $N(\text{H I})$. Indeed, according to radiation-transfer modelling by Ver-

hamme et al. (2015), $V_{\text{sep}} = 199 \text{ km s}^{-1}$ would correspond to $N(\text{H I}) \lesssim 10^{18} \text{ cm}^{-2}$, as predicted by some models, enabling an efficient leakage of LyC photons.

9 CONCLUSIONS

In this paper we present new *Hubble Space Telescope* (HST) Cosmic Origins Spectrograph (COS) observations of the compact star-forming galaxy (SFG) J1154+2443 with a high $\text{O}_{32} = [\text{O III}]\lambda 5007/[\text{O II}]\lambda 3727$ flux ratio ~ 11.5 , and a redshift $z = 0.3690$, aimed at studying its Ly α emission and escaping Lyman continuum (LyC) radiation. This study is a continuation of a project started by Izotov et al. (2016a,b). Our main results are as follows:

1. Escaping LyC radiation is detected in J1154+2443 with the highest escape fraction $f_{\text{esc}}(\text{LyC}) = 46 \pm 2$ per cent found so far in a low-redshift SFG.

2. A double-peaked Ly α emission line is observed in the spectrum of J1154+2443 with the separation between the blue and red peaks V_{sep} of 199 km s^{-1} , the lowest known so far for Ly α -emitting galaxies. Comparing the extinction-corrected Ly α /H β flux ratio with the case B value, we obtain an escape fraction $f_{\text{esc}}(\text{Ly}\alpha) \sim 98$ per cent, among the highest known for LAEs. Following Verhamme et al. (2017) we also find a strong anticorrelation between the f_{esc} and V_{sep} .

3. The COS near ultraviolet (NUV) acquisition images reveal a bright star-forming region in the centre of the galaxy and an exponential disc at the outskirts, with a disc scale length of ~ 1.09 kpc, indicating that J1154+2443 is a dwarf disc system.

4. J1154+2443 is characterized by a high star-formation rate $\text{SFR} = 18.9 M_{\odot} \text{ yr}^{-1}$ and a stellar mass $M_{\star} = 10^{8.20} M_{\odot}$. Its specific star formation rate of $1.2 \times 10^{-7} \text{ yr}^{-1}$ is one of the highest among the known nearby LyC leakers. The metallicity of J1154+2443, accurately determined from the optical emission lines is $12 + \log(\text{O}/\text{H}) = 7.65$, the lowest among the known low-redshift LyC leakers.

5. The observations demonstrate that a selection for compact high-excitation star-forming galaxies showing a high O_{32} ratio picks up very efficiently sources with significant Lyman continuum emission. Together with results by Izotov et al. (2016a,b), our results open effective ways to find and explore the sources of cosmic reionization.

ACKNOWLEDGEMENTS

Based on observations made with the NASA/ESA *Hubble Space Telescope*, obtained from the data archive at the Space Telescope Science Institute. STScI is operated by the Association of Universities for Research in Astronomy, Inc. under NASA contract NAS 5-26555. Support for this work was provided by NASA through grant number HST-GO-14635.001-A from the Space Telescope Science Institute, which is operated by AURA, Inc., under NASA contract NAS 5-26555. I.O. acknowledges grants GACR 14-20666P and 17-06217Y of the Czech National Foundation. Funding for SDSS-III has been provided by the Alfred P. Sloan Foundation, the Participating Institutions, the National Science Foundation, and the U.S. Department of Energy Office of Science. The SDSS-III web site is <http://www.sdss3.org/>. SDSS-III is managed

by the Astrophysical Research Consortium for the Participating Institutions of the SDSS-III Collaboration. GALEX is a NASA mission managed by the Jet Propulsion Laboratory. This research has made use of the NASA/IPAC Extragalactic Database (NED) which is operated by the Jet Propulsion Laboratory, California Institute of Technology, under contract with the National Aeronautics and Space Administration.

REFERENCES

- Ade P. A. R. et al., 2014, *A&A*, 571, A16
 Ahn C. P. et al., 2014, *ApJS*, 211, 17
 Aller L. H., 1984, *Physics of Thermal Gaseous Nebulae* (Dordrecht: Reidel)
 Bian F., Fan X., McGreer I., Cai Z., Jiang L., 2017, *ApJ*, 837, 12
 Borthakur S., Heckman T. M., Leitherer C., Overzier R. A., 2014, *Science*, 346, 216
 Boutsia K. et al., 2011, *ApJ*, 736, 41
 Bouwens R. J., Illingworth G. D., Oesch P. A., Caruana J., Holwerda B., Smit R., Wilkins S., 2015, *ApJ*, 811, 140
 Bouwens R. J., Illingworth G. D., Oesch P. A., Atek H., Lam D., Stefanon M., 2017, *ApJ*, 843, 41
 Calzetti D., Kinney A. L., Storchi-Bergmann T., 1994, *ApJ*, 429, 582
 Calzetti D., Armus L., Bohlin R. C., Kinney A. L., Koornneef J., Storchi-Bergmann T., 2000, *ApJ*, 533, 682
 Cardamone C. et al., 2009, *MNRAS*, 399, 1191
 Cardelli J. A., Clayton G. C., Mathis J. S., 1989, *ApJ*, 345, 245
 Chisholm J., Orlitová I., Schaerer D., Verhamme A., Worseck G., Izotov Y. I., Thuan T. X., Guseva N. G., 2017, *A&A*, 605, A67
 Cowie L. L., Barger A. J., Trouille L., 2009, *ApJ*, 692, 1476
 Curtis-Lake E. et al., 2016, *MNRAS*, 457, 440
 de Barros S. et al., 2016, *A&A*, 585, A51
 Deharveng J.-M., Buat V., Le Brun V., Milliard B., Kunth D., Shull J. M., Gry C., 2001, *A&A*, 375, 805
 Dressler A., Henry A., Martin C. L., Sawicki M., McCarthy P., Villaneuva E., 2015, *ApJ*, 806, 19
 Faisst A. L., 2016, *ApJ*, 829, 99
 Ferland G. J., Korista K. T., Verner D. A., Ferguson J. W., Kingdon J. B., Verner E. M., 1998, *PASP*, 110, 761
 Ferland G. J. et al., 2013, *Revista Mexicana Astronomy and Astrophysics*, 49, 137
 Girardi L., Bressan A., Bertelli G., Chiosi C., 2000, *A&AS*, 141, 371
 Grazian A. et al., 2016, *A&A*, 585, A48
 Green J. C. et al., 2012, *ApJ*, 744, 60
 Grimes, J. P. et al., 2009, *ApJ*, 181, 272
 Guseva N. G., Izotov Y. I., Fricke K. J., Henkel C., 2013, *A&A*, 555, A90
 Hanuschik R. W., 2003, *A&A*, 407, 1157
 Hassan S., Davé R., Mitra S., Finlator K., Ciardi B., Santos M. G., 2018, *MNRAS*, 473, 227
 Heap S. R. et al., 1995, *PASP*, 107, 871
 Henry A., Scarlata C., Martin C. S., Erb D., 2015, *ApJ*, 809, 19
 Inoue A. K., Shimizu I., Iwata I., Tanaka M., 2014, *MNRAS*, 442, 1805

- Iwata I. et al., 2009, *ApJ*, 692, 1287
- Izotov Y. I., Thuan T. X., Lipovetsky V. A., 1994, *ApJ*, 435, 647
- Izotov Y. I., Stasińska G., Meynet G., Guseva N. G., Thuan T. X., 2006, *A&A*, 448, 955
- Izotov Y. I., Guseva N. G., Thuan T. X., 2011, *ApJ*, 728, 161
- Izotov Y. I., Stasińska G., Guseva N. G., 2013, *A&A*, 558, A57
- Izotov Y. I., Guseva N. G., Fricke K. J., Henkel C., 2015, *MNRAS*, 451, 2251
- Izotov Y. I., Orlitová I., Schaerer D., Thuan T. X., Verhamme A., Guseva N. G., Worseck G., 2016a, *Nature*, 529, 178
- Izotov Y. I., Schaerer D., Thuan, T. X., Worseck G., Guseva N. G., Orlitová I., Verhamme A., 2016b, *MNRAS*, 461, 3683
- Izotov Y. I., Guseva N. G., Fricke K. J., Henkel C., 2016c, *MNRAS*, 462, 4427
- Izotov Y. I., Thuan T. X., Guseva N. G., 2017, *MNRAS*, 471, 548
- Jaskot A. E., Oey M. S., 2013, *ApJ*, 766, 91
- Jaskot A. E., Oey M. S., 2014, *ApJ*, 791, L19
- Kennicutt R. C., Jr., 1998, *Ann.Rev.Astron.Astrophys.*, 36, 189
- Khaire V., Srianand R., Choudhury T. R., Gaikwad P., 2016, *MNRAS*, 457, 4051
- Leitet E., Bergvall N., Hayes M., Linné S., Zackrisson E., 2013, *A&A*, 553, A106
- Leitherer C., Ferguson H. C., Heckman T. M., Lowenthal J. D., 1995, *ApJ*, 454, L19
- Leitherer C. et al., 1999, *ApJS*, 123, 3
- Leitherer C., Ekström S., Meynet G., Schaerer D., Agienko K. B., Levesque E. M., 2014, *ApJS*, 212, 14
- Leitherer C., Hernandez S., Lee J. C., Oey M. S., 2016, *ApJ*, 823, L64
- Lejeune T., Buser R., Cuisinier F., 1997, *A&AS*, 125, 229
- Madau P., Haardt F., 2015, *ApJL*, 813, L8
- Mathis J. S., 1990, *Ann.Rev.Astron.Astrophys.*, 28, 10
- Mitra S., Ferrara A., Choudhury T. R., 2013, *MNRAS*, 428, L1
- Mitra S., Choudhury T. R., Ferrara A., 2018, *MNRAS*, 473, 1416
- Mostardi R. E., Shapley A. E., Nestor D. B., Steidel C. C., Reddy N. A., Trainor R. F., 2013, *ApJ*, 779, 65
- Murthy J., 2014, *ApJS*, 213, 32
- Nakajima K., Ouchi M., 2014, *MNRAS*, 442, 900
- Nestor D. B., Shapley A. E., Steidel C. C., Siana B., 2011, *ApJ*, 736, 18
- Ouchi M. et al., 2009, *ApJ*, 706, 1136
- Paulino-Afonso A. et al., 2017, *MNRAS*, in press; preprint arXiv:1709.04470
- Robertson B. E. et al., 2013, *ApJ*, 768, 71
- Robertson B. E., Ellis R. S., Furlanetto S. R., Dunlop J. S., 2015, *ApJL*, 802, L19
- Salpeter E. E., 1955, *ApJ*, 121, 161
- Schaerer D., Izotov Y. I., Verhamme A., Orlitová I., Thuan T. X., Worseck G., Guseva, N. G., 2016, *A&A*, 591, L8
- Schmutz W., Leitherer C., Gruenwald, R., 1992, *PASP*, 104, 1164
- Shapley A. E., Steidel C. C., Strom A. L., Bogosavljević M., Reddy N. A., Siana B. Mostardi R. E., Rudie G. C., 2016, *ApJ*, 826, L24
- Stasińska G., Izotov Y., Morisset C., Guseva N., 2015, *A&A*, 576, A83
- Steidel C. C., Pettini M., Adelberger K. L., 2011, *ApJ*, 546, 665
- Vanzella E. et al., 2010, *ApJ*, 725, 1011
- Vanzella E. et al., 2012, *ApJ*, 751, 70
- Vanzella E. et al., 2015, *A&A*, 576, A116
- Verhamme A., Orlitová I., Schaerer D., Hayes M., 2015, *A&A*, 578, A7
- Verhamme A., Orlitová I., Schaerer D., Izotov Y., Worseck G., Thuan T. X., Guseva N., 2017, *A&A*, 597, A13
- Wise J. H., Cen R., 2009, *ApJ*, 693, 984
- Worseck G., Prochaska J. X., Hennawi J. F., McQuinn M., 2016, *ApJ*, 825, 144
- Wright E. L., 2006, *PASP*, 118, 1711
- Yajima H., Choi J.-H., Nagamine K., 2011, *MNRAS*, 412, 411
- Yang H. et al., 2017, *ApJ*, 844, 171

APPENDIX A: COS BACKGROUND SUBTRACTION

As detailed in Appendix B of Worseck et al. (2016), the COS background is composed of dark current, scattered light (mostly scattered geocoronal emission), and the diffuse UV sky background. At the sensitivity limit of *HST*/COS, the accuracy of our flux measurements may be limited by the accuracy of the estimated total background counts $B = B_{\text{dark}} + B_{\text{scatter}} + B_{\text{sky}}$ during the exposure. The dark current B_{dark} varies with time, mostly due to variations of the thermospheric density at *HST*'s altitude with the solar cycle, but also due to changes in the cosmic ray flux with the Earth's magnetic field in *HST*'s orbit. Worseck et al. (2016) found that the COS detector pulse height distribution of the dark current is sensitive to the ambient conditions, and that it traces the spatial structure of the dark current across the detector. Thus, while COS detector gain sag prevents a direct estimation of the dark current in the science extraction aperture, it can be modelled in post-processing by matching the pulse height distributions in unilluminated detector regions of the science exposures to those of contemporary dark current monitoring exposures.

Specifically, for our COS G140L data obtained at COS Lifetime Position 3 we chose two 50-pixel wide unilluminated regions above and below the trace (geometrically corrected spatial coordinates $379 < y < 429$ and $502 < y < 552$), avoiding spectral ranges affected by scattered geocoronal emission, grid wires and detector blemishes. In the left panels of Fig. A1 we compare the cumulative pulse height distributions in the calibration regions of the four science exposures to those same regions in 40 dark monitoring exposures (Programme 14520) obtained within ± 1 month of the science observations. We characterised their difference by computing the maximum absolute difference in the cumulative distributions

$$D = \max_k |F_{\text{dark}}(< k) - F_{\text{science}}(< k)|, \quad (\text{A1})$$

where F_{dark} and F_{science} are the empirical cumulative distributions to pulse height amplitude $0 \leq k \leq 31$. Due to low

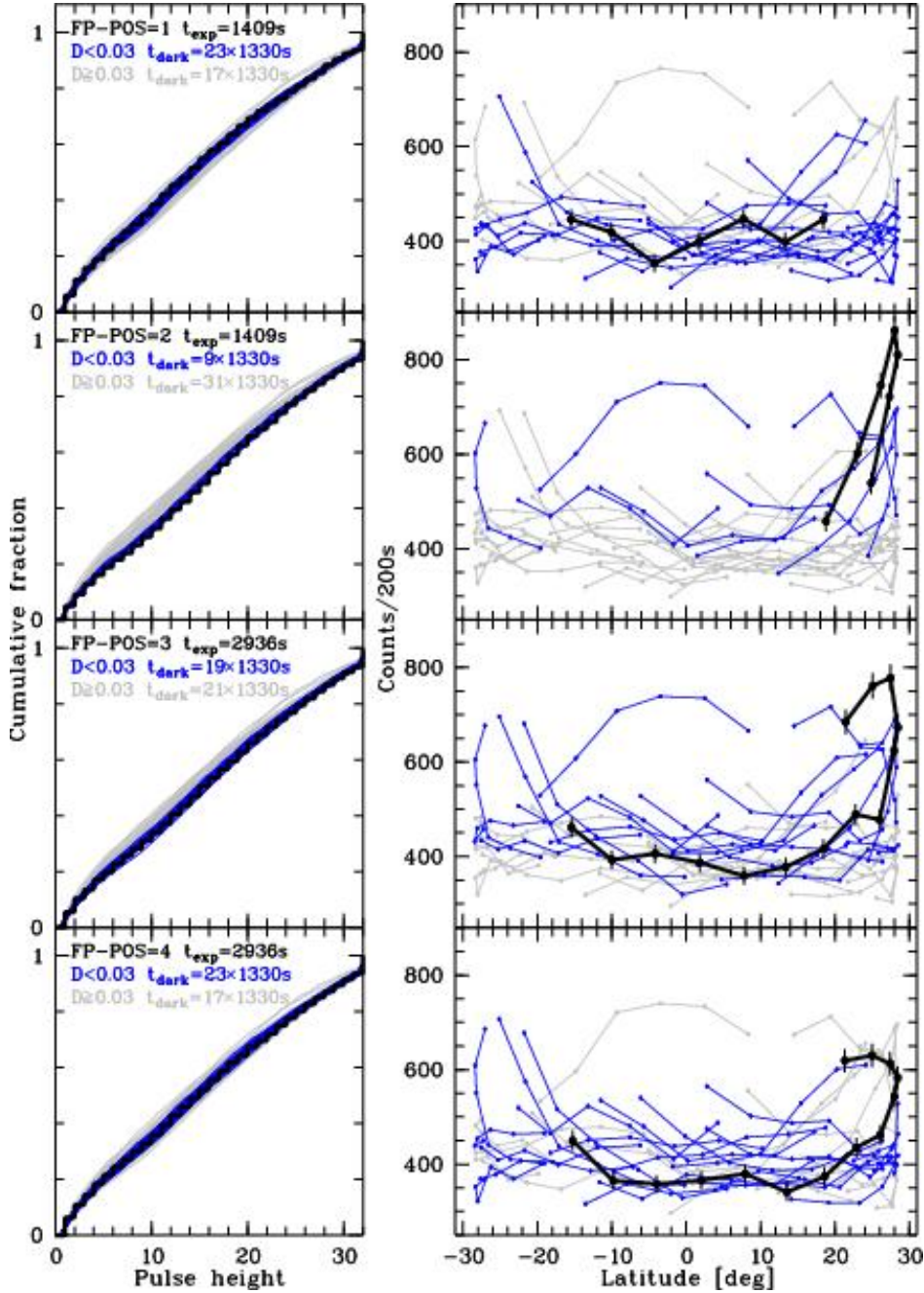


Figure A1. *Left:* Cumulative pulse height distributions in the chosen calibration windows on COS detector segment A for the four G140L science exposures of J1154+2443 (thick black) and for 40 dark exposures obtained within ± 1 month of the science observation date. Blue lines show dark exposures with a pulse height distribution similar to the one of the science exposure ($D < 0.03$), whereas grey lines show rejected dark exposures ($D \geq 0.03$). *Right:* Corresponding total counts in the calibration windows measured in regular 200 s time intervals of the exposure as a function of latitude in *HST*'s orbit. For J1154+2443 we also plot Poisson errors of the counts.

solar activity in the sampled time interval the pulse height distributions are quite similar, with remaining small differences due to varying local ambient conditions. We chose a threshold $D < 0.03$ to combine the dark exposures obtained in similar conditions to the science exposures, treating science exposures individually. The dark current was extracted in the chosen science aperture with the same pulse height thresholds as for the science data, and smoothed with a 500-pixel running average to capture variations in the dark cur-

rent along the dispersion axis, avoiding grid wires and detector blemishes. Finally, the smoothed dark current was scaled to the science exposure via the ratio of the total counts in the calibration regions. The dark current was co-added together with the science exposures, accounting for focal plane offsets and propagating statistical errors of the scaling factors and Poisson errors in the smoothed darks. The final dark current estimate is accurate to a few per cent.

The right panels in Fig. A1 show the total counts in the

Table A1. Counts and estimated backgrounds in the extraction aperture in the rest-frame wavelength range 830–850 Å

No. of exposure	t_{exp} [s]	N^a	B_{dark}^b	B_{scatter}^c	B_{sky}^d	B^e
1	1409.184
2	1409.184	58	10.30 ± 0.77	2.08 ± 0.25	0.48 ± 0.05	12.86 ± 1.07
3	2936.160	200	29.86 ± 1.61	16.32 ± 1.96	1.67 ± 0.17	47.85 ± 3.74
4	2936.192	213	27.76 ± 1.47	16.57 ± 1.99	1.75 ± 0.18	46.08 ± 3.64
total	8690.712	471	67.92 ± 3.85	34.97 ± 4.20	3.89 ± 0.39	106.78 ± 8.44

^aTotal number of counts (object+background).

^bCounts of the dark current.

^cCounts of the scattered light (mostly scattered geocoronal emission).

^dCounts of the diffuse UV sky background.

^eTotal number of the background counts.

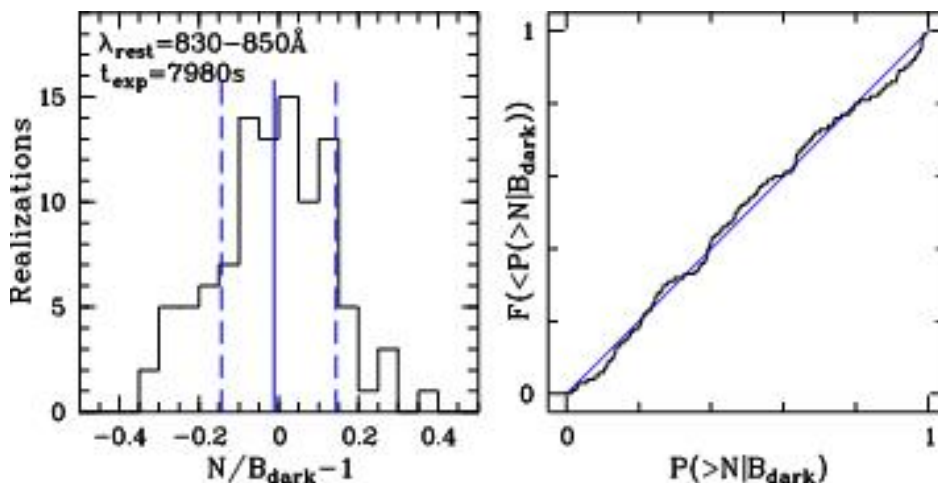


Figure A2. *Left:* Relative deviation between measured dark counts N and estimated dark current B_{dark} for random subsamples of 6/60 dark exposures obtained 2017 June 5 – August 21 in the aperture and wavelength range used to measure the LyC flux. The solid and dashed lines show the mean and the standard deviation of the 100 realizations, respectively. *Right:* Cumulative fraction $F(< P(> N | B_{\text{dark}}))$ of Poisson probabilities $P(> N | B_{\text{dark}})$ to detect more than N dark counts given the dark current B_{dark} for the 100 realizations. The blue line marks identity.

calibration regions obtained in regular 200 s intervals during the exposure as a function of geographic latitude of *HST* in its orbit. The dark current increases from low to high geographic latitude by ~ 50 per cent, but with statistically significant scatter even at the well-sampled low latitudes. The increase at high geographic latitudes is most likely due to the increased cosmic ray flux at high geomagnetic latitudes (see e.g. Heap et al. 1995, for measurements with *HST*/GHRS). The scatter at fixed geographic latitude is due to the tilt between the geomagnetic axis and Earth’s rotation axis, but also due to longitudinal features in the Earth’s magnetic field, such as the South Atlantic Anomaly. Thus, part of the variation in the average dark count rate measured in the dark monitoring programme is due to different orbit parameters and locations sampled by the observations, in addition to the much larger variation during solar activity (low in the time interval sampled in Fig. A1). Due to the sparse dark current monitoring (5×1330 s per week) randomly sampling the part of the magnetosphere traversed by *HST* in its orbit, it is likely impossible to obtain a sufficiently accurate map of the dark current as a function of geomagnetic coordinates, even when averaging over long time intervals during solar minimum. Therefore, we approximated the dark cur-

rent during the science observations with dark monitoring data obtained at vastly different locations but with a similar pulse height distribution. Accounting for the difference in exposure times (i.e. the range in latitude) Fig. A1 indicates that our threshold $D < 0.03$ selects darks obtained at similar latitude as the science observations.

We tested our approach by treating random subsets of 6 out of 60 dark exposures obtained between June and August 2017 as science data, with the remainder taken for calibration (e.g. Worseck et al. 2016). Focal plane offsets were emulated (1330 s at offset positions 1 and 2, 2×1330 s at positions 3 and 4), such that the co-added spectrum had a pixel exposure time distribution very similar to the G140L data of J1154+2443. We used the same calibration regions and pulse height range as in the science reductions. The left panel of Fig. A2 shows the relative deviation between the measured dark counts and the estimated dark current in the aperture and wavelength range of our LyC flux measurement in J1154+2443. From 100 realizations we obtain a mean relative deviation -0.012 , showing that our procedure estimates the dark current with insignificant systematic error (see also Worseck et al. 2016; Chisholm et al. 2017). The rather large standard deviation of 0.144 is due to Poisson fluctuations

of the measured dark counts around the mean $B_{\text{dark}} \simeq 50$ counts⁴. To test this we computed the Poisson probability

$$P(> N|B_{\text{dark}}) = 1 - \sum_{k=0}^N \frac{B_{\text{dark}}^k e^{-B_{\text{dark}}}}{k!} \quad (\text{A2})$$

of measuring more than the N registered counts given the estimated dark current B_{dark} , and compared that number to the fraction of the 100 realizations with smaller P values (Worseck et al. 2016). The right panel of Fig. A2 shows that the empirical cumulative distribution approximately follows the expectation for a Poisson distribution, in particular in the tails of strong over- and undersubtraction of the dark current. This analysis also confirms that the dark current of a particular exposure can be modelled satisfactorily with dark exposures obtained at different locations.

As a result, Equation A2 estimates the probability that the measured counts $N > B$ are consistent with a Poisson fluctuation of the background B . The scattered light and its uncertainty was estimated following Worseck et al. (2016), whereas the diffuse sky background was taken from Murthy (2014) with an estimated uncertainty of 10 per cent. Table A1 lists the total counts and the estimated background components in the rest-frame wavelength range used for our LyC flux measurement in J1154+2443. Note that due to the focal plane offsets and the grid wires the actual spectral coverage differs among the four exposures. The detected counts significantly exceed the total estimated background in every exposure, and the estimated background uncertainty does not affect this result. In the co-added exposure, it is highly unlikely that the measured 471 counts in the LyC are entirely due to the total background ($P(> N|B) < 10^{-7}$ eventually limited by the assumption in Equation A2). Even assuming a background higher by a factor 3.5 would not change this result ($P(> N|B) = 5.4 \times 10^{-7}$).

This paper has been typeset from a $\text{\TeX}/\text{\LaTeX}$ file prepared by the author.

⁴ The estimated B_{dark} varies depending on the chosen subset of darks treated as science exposures.